An engineered PET depolymerase to break down and recycle plastic bottles

https://doi.org/10.1038/s41586-020-2149-4

Received: 27 June 2019

Accepted: 19 February 2020

Published online: 8 April 2020

Check for updates

V. Tournier[1,4], C. M. Topham[1,4], A. Gilles[1], B. David[1], C. Folgoas[1], E. Moya-Leclair[1], E. Kamionka[1], M.-L. Desrousseaux[1], H. Texier[1], S. Gavalda[1], M. Cot[2], E. Guémard[3], M. Dalibey[3], J. Nomme[1], G. Cioci[1], S. Barbe[1], M. Chateau[3], I. André[1]✉, S. Duquesne[1]✉ & A. Marty[1,3]✉

Present estimates suggest that of the 359 million tons of plastics produced annually worldwide[1], 150–200 million tons accumulate in landfill or in the natural environment[2]. Poly(ethylene terephthalate) (PET) is the most abundant polyester plastic, with almost 70 million tons manufactured annually worldwide for use in textiles and packaging[3]. The main recycling process for PET, via thermomechanical means, results in a loss of mechanical properties[4]. Consequently, de novo synthesis is preferred and PET waste continues to accumulate. With a high ratio of aromatic terephthalate units—which reduce chain mobility—PET is a polyester that is extremely difficult to hydrolyse[5]. Several PET hydrolase enzymes have been reported, but show limited productivity[6,7]. Here we describe an improved PET hydrolase that ultimately achieves, over 10 hours, a minimum of 90 per cent PET depolymerization into monomers, with a productivity of 16.7 grams of terephthalate per litre per hour (200 grams per kilogram of PET suspension, with an enzyme concentration of 3 milligrams per gram of PET). This highly efficient, optimized enzyme outperforms all PET hydrolases reported so far, including an enzyme[8,9] from the bacterium *Ideonella sakaiensis* strain 201-F6 (even assisted by a secondary enzyme[10]) and related improved variants[11–14] that have attracted recent interest. We also show that biologically recycled PET exhibiting the same properties as petrochemical PET can be produced from enzymatically depolymerized PET waste, before being processed into bottles, thereby contributing towards the concept of a circular PET economy.

Given that crystalline PET has been found to be subject to only limited depolymerization by cutinase enzymes[8,15–17], we used a commercially available amorphous PET (Gf-PET, from the supplier Goodfellow) to compare the activity of several enzymes reported previously to hydrolyse PET in their optimal conditions. These enzymes were *Thermobifida fusca* hydrolases 1 and 2 (BTA1 and BTA2), *Fusarium solani pisi* cutinase (FsC), *Ideonella sakaiensis* PETase (Is-PETase) and leaf-branch compost cutinase (LCC) (Extended Data Fig. 1a, b). LCC outperformed all other enzymes tested, reaching an initial PET-specific depolymerization rate of 93.2 $mg_{TAeq.}\ h^{-1}\ mg_{enzyme}^{-1}$ at 65 °C (Fig. 1a; 'TAeq.' refers to equivalents of terephthalic acid, as detailed in Supplementary Method 1). We found LCC to be at least 33 times more efficient than any other enzyme tested (Fig. 1a and Extended Data Fig. 1b), while also demonstrating the highest thermostability, with a determined melting temperature of 84.7 °C (Extended Data Fig. 1a). This depolymerization performance of LCC at 65 °C was slightly lower when using bottle-grade PET (Pf-PET) as a substrate (Fig. 1a and Extended Data Fig. 1b), with an initial PET-specific depolymerization rate of 81.9 $mg_{TAeq.}\ h^{-1}\ mg_{enzyme}^{-1}$. While approaching the glass transition temperature, known to maximize PET chain mobility and enzymatic depolymerization[18,19], the LCC reaction stopped after 3 days at 65 °C with a Pf-PET conversion level of only 31% (Fig. 1b). We observed no inhibition by the depolymerization products ethylene glycol and terephthalic acid at the concentrations that would be obtained at 100% Pf-PET depolymerization (Extended Data Fig. 2a), and Pf-PET crystallinity was unchanged after 6 days at 65 °C (10% crystallinity, as measured by differential scanning calorimetry). Moreover, the initial kinetics could be restored by adding LCC to the stopped reaction (Extended Data Fig. 2b), implying that the thermostability of LCC was most likely to be the limiting factor, notwithstanding its high melting temperature when free in solution. To optimize depolymerization yields, we sought to improve both the activity and the thermostability of LCC through enzyme engineering.

To identify amino acid residues for mutagenesis to improve catalytic activity, we used molecular docking and enzyme contact-surface analysis to investigate the mode of binding of a model substrate, 2-HE$(MHET)_3$, in the active site of wild-type LCC (Protein Data Bank (PDB; https://www.rcsb.org) ID 4EB0). We found that the substrate binds in an elongated and predominantly hydrophobic groove (Fig. 2a) present in all X-ray structures of prokaryotic cutinases reported to date[20–22]. In total, we identified 15 amino acid residues in the first contact shell, of which we chose 11 for targeted mutagenesis (Extended Data Table 1). We subjected these 11 positions to site-specific saturation mutagenesis to generate all possible 209 variants. Most variants showed impaired depolymerization of Pf-PET: more than 25% of the

[1]TBI, Université de Toulouse, CNRS, INRAE, INSA, Toulouse, France. [2]CRITT Bio-Industries, INSA, Toulouse, France. [3]Carbios, Biopôle Clermont Limagne, Saint-Beauzire, France. [4]These authors contributed equally: V. Tournier, C. M. Topham. ✉e-mail: isabelle.andre@insa-toulouse.fr; sophie.duquesne@insa-toulouse.fr; alain.marty@carbios.fr

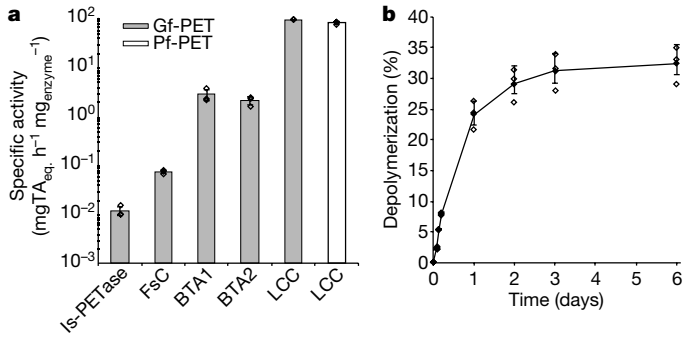

Fig. 1 | LCC outperformed all other evaluated PET hydrolases during PET-depolymerization assays. a, Comparison of the specific hydrolysis activity towards amorphous Gf-PET by: Is-PETase or FsC in 50 mM glycine NaOH buffer, pH 9, at 40 °C; BTA-hydrolase 1 or BTA-hydrolase 2 (BTA1 and BTA2 respectively) in 1 M potassium phosphate buffer, pH 8, at 65 °C; and LCC in 100 mM potassium phosphate buffer, pH 8, at 65 °C. The hydrolysis of Pf-PET by LCC in 100 mM potassium phosphate buffer, pH 8, at 65 °C is also shown. Equimolar amounts of purified proteins were used (6.9 nmol$_{protein}$ g$_{PET}^{-1}$ and 2 g$_{PET}$ l$_{buffer}^{-1}$). Means ± s.d. (n = 3) are shown. **b**, Detailed hydrolysis kinetics for Pf-PET depolymerization by LCC, as described in **a**. Each filled symbol represents the mean ± s.d. (n = 3).

variants exhibited less than 1% specific activity by comparison with wild-type LCC, and more than 75% exhibited less than 48% specific activity (Extended Data Fig. 3a). Variants with 75% or more activity compared with wild-type LCC were purified and analysed individually for Pf-PET depolymerization specific activity and determination of the melting temperature by differential scanning fluorimetry (DSF). Of 25 such variants, we selected variants I and W of the F243 position for further analysis, as they showed improved activity versus wild-type LCC (Fig. 2b); we also highlighted variants T96M, Y127G, N246D and N246M, which exhibited an increased melting temperature, although no improvement in Pf-PET depolymerization activity (Extended Data Fig. 3b).

To improve the thermostability of LCC, we sought divalent-metal-binding sites known to increase enzyme thermal stability in PET hydrolases[23,24]. No such metal-ion-binding site could be directly observed in the 1.5 Å X-ray structure of LCC[25]. However, such a site—formed by the side chains of three acidic amino acid residues—can be identified at topologically equivalent positions in the X-ray structures of three cutinase homologues (Fig. 3a). The corresponding residue triplet in LCC comprises two acidic residues (E208 and D238) and the neutral S283 (Fig. 3a). DSF experiments confirmed that LCC was thermally stabilized by the addition of calcium ions (the melting temperature increased by 9.3 °C on addition of 35 mM $CaCl_2$), in accordance with previous results[25] (Fig. 3b). However, in order to reduce reaction costs and the need for extensive downstream purification, we preferred to avoid salts and additives. We adopted the alternative strategy of replacing the divalent-metal-binding site with a disulfide bridge[26]. The Cα–Cα (4.5 Å) and Cβ–Cβ (4.4 Å) interatomic separation distances for the D238 and S283 residue pair in the LCC X-ray structure were compatible with the engineering of a disulfide bridge[27]. A D238C/S283C variant was produced and disulfide-bond formation verified by DSF (Extended Data Fig. 4), allowing thermal stabilization of LCC without dependence on calcium ions (Fig. 3b). This variant exhibited a melting temperature of 94.5 °C (9.8 °C higher than that of wild-type LCC), with a decrease in activity of only 28% (Extended Data Fig. 3b).

We added the two mutations leading to the highest specific activity to the new thermostable variant. The resulting F243I/D238C/S283C (ICC) and F243W/D238C/S283C (WCC) variants restored the activity of the D238C/S283C variant to at least wild-type LCC levels (122% and 98%, respectively), with melting temperatures that were 6.2 °C and 10.1 °C higher, respectively (Extended Data Fig. 3b). Subsequently, we added T96M, Y127G, N246D or N246M mutations—shown to improve thermostability—to ICC and WCC, generating eight new variants. After comparative analysis of specific activities and melting temperatures (Extended Data Fig. 3b), we selected variants F243I/D238C/S283C/Y127G (ICCG), F243I/D238C/S283C/N246M (ICCM), F243W/D238C/S283C/Y127G (WCCG) and F243W/D238C/S283C/N246M (WCCM), as they retained specific activity that was similar to or higher than that of wild-type LCC, with improved melting temperatures ranging from +9.3 °C to +13.4 °C.

To enable a scale-up of the process, we evaluated these four quadruple variants (ICCG, ICCM, WCCG and WCCM) in bioreactor conditions and using post-consumer coloured-flake PET waste (PcW-PET). This PcW-PET is the under-valorized residue remaining after the ultimate sorting that leads to clear PET waste (the latter being used for the thermomechanical process of PET recycling). We raised the concentration of PcW-PET to 200 g kg^{-1} of the total weight of the reaction volume (PET plus liquid phase) in order to maximize reactor productivity. We applied pretreatment technologies (extrusion and micronization) that are widely used by plastic industries[28,29] to amorphize and increase the exchange surface of PcW-PET, performing this pretreatment on a ton-scale here. We raised the temperature to 72 °C in order to maximize kinetic turnover (Fig. 4), 75 °C being detrimental to PET conversion (Extended Data Fig. 5a) owing to rapid recrystallization of PcW-PET. Indeed, 24.7% crystallinity was reached in 9 h at 72 °C, whereas it took only 6 h to reach its maximal 37.5% at 75 °C (Extended Data Fig. 6). The best conversion level was obtained with ICCG and WCCG, achieving 82% and 85% conversion in 20 h and 15 h respectively (Fig. 4a). Wild-type LCC, which shows reduced thermostability compared with the ICCG and WCCG variants (resulting in a rapid decrease in reaction kinetics after 2 h), reached only 53% conversion in 20 h. The remaining 47% of PcW-PET had a high level of crystallinity, estimated at 28.9%, making an immediate reuse for PET depolymerization unsuitable.

As a ratio of 3 milligrams of enzyme per gram of PET appeared to maximize PcW-PET depolymerization (Extended Data Fig. 5b), we compared ICCG and WCCG at this ratio. Under these conditions, 90% depolymerization was obtained for both WCCG and ICCG variants in 10.5 h and 9.3 h, respectively (Fig. 4b). For the ICCG variant, a higher initial rate was observed (Extended Data Fig. 5c), and we determined a maximum specific space-time-yield of 70.1 g$_{TA}$ l^{-1} h^{-1} g$_{enzyme}^{-1}$ (27.9 g$_{TA}$ l^{-1} h^{-1} g$_{enzyme}^{-1}$ over the course of the reaction), corresponding to a maximum productivity of 42.1 g$_{TA}$ l^{-1} h^{-1} (16.7 g$_{TA}$ l^{-1} h^{-1} over the course of the reaction). This mean productivity was 98-fold higher than the productivity reported previously by using TfCut2 with amorphous PET[17]. Notably, it is also considerably higher than the productivity reported during degradation of starch[30] (4 g l^{-1} h^{-1}) or cotton[31] (0.31 g l^{-1} h^{-1}). To enable the scientific community to use this enzyme as a reference, we assayed its performance with commercially available Gf-PET in laboratory-scale conditions (as described in Supplementary Method 1); the initial rate was 105.6 ± 3.9 mg$_{TAeq.}$ h^{-1} mg$_{enzyme}^{-1}$. To gain better insight into the structural effects of the mutations, we combined X-ray crystallography (Extended Data Table 2 and Extended Data Fig. 7) and molecular-dynamics simulations of the enzymes. In the free state (Extended Data Fig. 8a), no substantial difference was observed between parental LCC and ICCG. Conversely, molecular-dynamics simulations of the ICCG variant in complex with the 2-HE(MHET)$_3$ model substrate (Extended Data Fig. 8b, c) revealed that the mutations introduced in ICCG facilitate the catalytically productive binding of 2-HE(MHET)$_3$ compared with parental LCC (Extended Data Fig. 8b, c). Accordingly, molecular mechanics/generalized Born surface area (MM/GBSA) calculations predicted an increased affinity of ICCG towards 2-HE(MHET)$_3$ ($\Delta\Delta G$ = −1.37 kcal mol^{-1}).

As a compromise between productivity and enzyme cost, we used the optimized ICCG variant at 2 mg g$_{PET}^{-1}$ in a 150-l pilot-scale depolymerization at a very high PcW-PET content (200 g kg^{-1}). We calculate that the cost of enzyme needed to recycle 1 ton of PET represents approximately

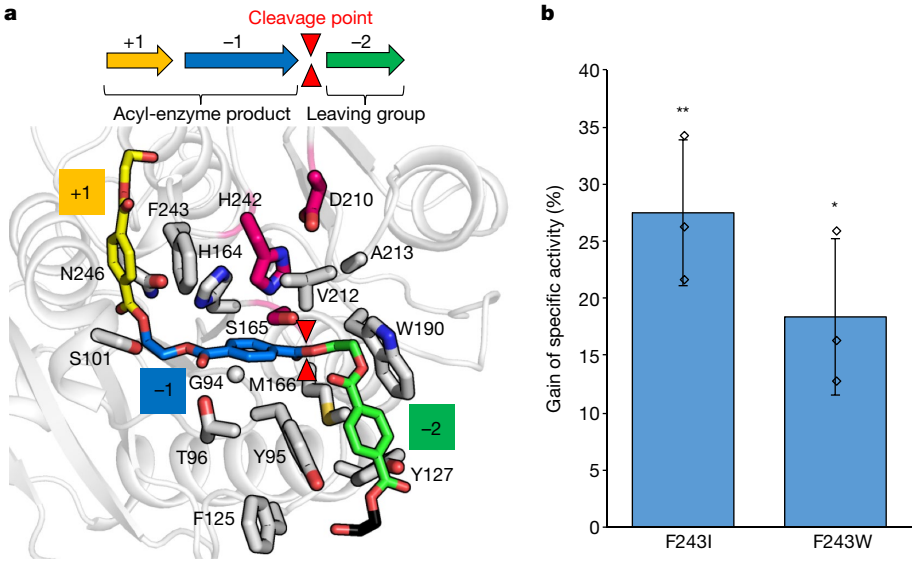

Fig. 2 | Improvement of the PET-depolymerization specific activity of LCC after mutagenesis by saturation of the residues in contact with a 2-HE(MHET)$_3$ substrate. a, Structural model of 2-HE(MHET)$_3$ (coloured stick model) docked in wild-type LCC (grey ribbon). The putative substrate-binding site of LCC can be subdivided into three subsites (−2, −1, +1), each in contact with the MHET units numbered relative to the scissile ester bond (red triangles). Amino acids in the first contact shell of LCC are shown as grey rods. Catalytic residues are in magenta. **b**, Calculated percentage improvement in specific activity of Pf-PET depolymerization by the F243I and F243W variants compared with wild-type LCC at 65 °C (6.9 nmol$_{protein}$ g_{PET}^{-1} and 2 g_{PET} l_{buffer}^{-1}). Means ± s.d. (n = 3) are shown; *P < 0.025; **P < 0.005 (one-sided t-test).

4% of the ton-price of the virgin PET, with a production cost of US$25 per kilogram of protein estimated using the cost of production of a cellulase in *Trichoderma reesei* ($5–$23 per kilogram of protein[32]).

As a first step of process development, we recycled only the terephthalic acid that represents the main part of the PET in weight (1 ton of PET waste leads to 863 kg of terephthalic acid). Using industrially relevant processes (namely discolouration by activated carbon, commonly used in large-scale processes[33], and crystallization, the final step for the chemical production of terephthalic acid[34]), we purified terephthalic acid monomers to a level higher than 99.8%, with an American Public Health Association (APHA) colour number of 2.9. During this process, 0.6 kg of sodium sulfate was produced per kg of recycled PET. With our new process, the recycling of 100,000 tons of PET per year will produce around 60,000 tons of sodium sulfate per year, representing 0.28% of the world market of sodium sulfate (21.5 million tons per year, especially in the detergent, paper and glass industries, with a 2.9%

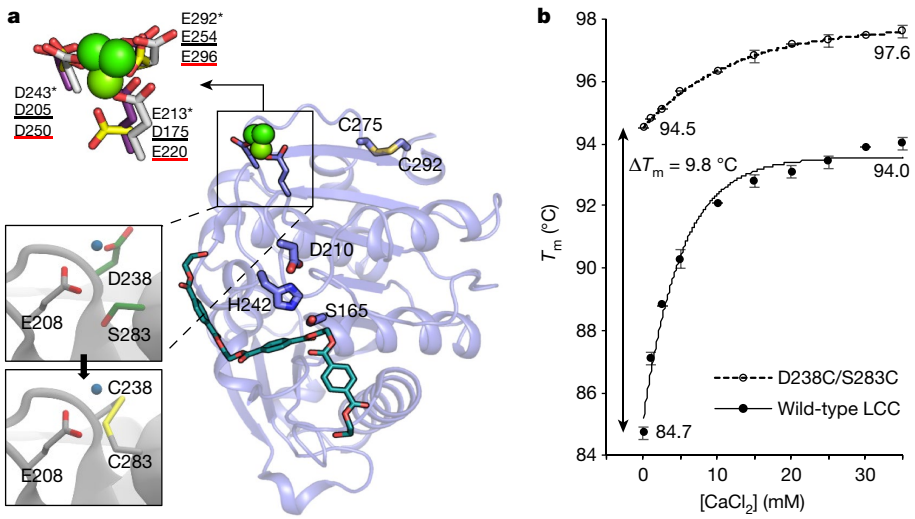

Fig. 3 | Improvement of LCC thermostability by addition of a disulfide bridge. a, The main figure shows locations of putative sites that coordinate divalent metal ions in the crystal structures of identified PET hydrolases. On wild-type LCC (ribbon), catalytic residues (S165, D210 and H242) and the C-terminal disulfide bond (C275–C292) are shown as blue rods. Divalent metal ions are shown as green spheres. In the upper inset, residues that bind metal ions in *Thermobifida alba* Est119 (PDB ID 3WYN) are shown as purple sticks, with the residues indicated with an asterisk; metal-binding residues in *Thermobifida cellulosilytica* Thc Cut1 (PDB ID 5LUI) are shown as yellow sticks, with the residues underlined in black; and the metal-binding sites in *Saccharomonospora viridis* Cut190 variants (PDB ID 4WFJ and 5ZNO) are shown as grey sticks, with residue names underlined in red. The left panels show a putative calcium-binding site formed by E208, D238 and S283 in LCC (with calcium shown as a blue sphere), and the disulfide bond (yellow) introduced here. **b**, Assessment of melting temperature (T_m) by DSF for both wild-type LCC and the D238C/S283C variant in the presence of increasing concentrations of $CaCl_2$. Curves represent the optimal fit to the data, and each symbol represents the mean ± s.d. (n = 3).

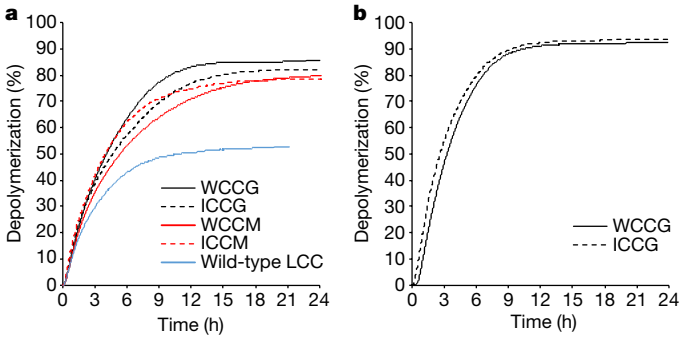

Fig. 4 | Improved performance of LCC variants in enzymatic depolymerization of post-consumer PET waste. Assays of PcW-PET (200 g kg^{-1}) depolymerization were carried out in Minibio bioreactors at pH 8 and 72 °C. **a**, Comparison of PcW-PET depolymerization kinetics at 1 mg_{enzyme} g_{PET}^{-1} for the WCCG, ICCG, WCCM and ICCM variants and wild-type LCC. **b**, Comparison of PcW-PET depolymerization kinetics at 3 mg_{enzyme} g_{PET}^{-1} for the WCCG and ICCG variants. PET-depolymerization percentages were calculated on the basis of NaOH consumption.

annual growth rate)[35]. We used the terephthalic acid produced here to synthesize virgin PET. During PET synthesis (in the polycondensation step), the levels of diethylene glycol, antimony and phosphorous and the value of carboxylic end groups were in the range of the bottle-grade PET norm (2.2%, 177 ppm, 14 ppm, 23 mg_{KOH} g^{-1}, respectively). At the end of the synthesis process (during solid-state polymerization), the evaluated number average molecular weight (36,650 g mol^{-1}) and intrinsic viscosity (0.75 dl g^{-1}) of the newly made PET were similar to those of PET synthesized using petrochemical terephthalic acid (evaluated number average molecular weight 38,390 g mol^{-1} and intrinsic viscosity 0.78 dl g^{-1}). Bottles blown from this PET had similar mechanical properties (a displacement of 2.9 mm at a maximal top-load force of 176 N) to those of commercial PET bottles (a displacement of 3.0 mm at a maximal top-load force of 181 N). Moreover, their excellent lightness values of 87.5% are better than those of the minimal standard for PET bottles (greater than 85%).

Here, using computer-aided enzyme engineering, we have improved enzyme-catalysed PET depolymerization to 90% conversion in less than 10 h, with a mean productivity of 16.7 g_{TA} l^{-1} h^{-1}. We have used the resulting purified terephthalic acid monomers to synthesize PET, which was ultimately blown into bottles, closing the loop of the circular economy. With the urgent global need to address the issue of plastic disposal—and with many governments, national and international agencies and manufacturers committing to sustainability goals and the idea of a circular economy—the enzymatic processing of PET waste described here may help to meet such goals.

Online content

Any methods, additional references, Nature Research reporting summaries, source data, extended data, supplementary information, acknowledgements, peer review information; details of author contributions and competing interests; and statements of data and code availability are available at https://doi.org/10.1038/s41586-020-2149-4.

1. PlasticsEurope. Plastics—the facts 2019. An analysis of European plastics production, demand and waste data. *PlasticsEurope* https://www.plasticseurope.org/application/files/1115/7236/4388/FINAL_web_version_Plastics_the_facts2019_14102019.pdf (2019).
2. Geyer, R., Jambeck, J. R. & Law, K. L. Production, use, and fate of all plastics ever made. *Sci. Adv.* **3**, e1700782 (2017).
3. PET polymer: chemical economics handbook. IHS Markit https://ihsmarkit.com/products/pet-polymer-chemical-economics-handbook.html (2018).
4. Ragaert, K., Delva, L. & Van Geem, K. Mechanical and chemical recycling of solid plastic waste. *Waste Manag.* **69**, 24–58 (2017).
5. Marten, E., Müller, R.-J. & Deckwer, W.-D. Studies on the enzymatic hydrolysis of polyesters. II. Aliphatic-aromatic copolyesters. *Polym. Degrad. Stabil.* **88**, 371–381 (2005).
6. Wei, R. & Zimmermann, W. Microbial enzymes for the recycling of recalcitrant petroleum-based plastics: how far are we? *Microb. Biotechnol.* **10**, 1308–1322 (2017).
7. Kawai, F., Kawabata, T. & Oda, M. Current knowledge on enzymatic PET degradation and its possible application to waste stream management and other fields. *Appl. Microbiol. Biotechnol.* **103**, 4253–4268 (2019).
8. Yoshida, S. et al. A bacterium that degrades and assimilates poly(ethylene terephthalate). *Science* **351**, 1196–1199 (2016).
9. Bornscheuer, U. T. Feeding on plastic. *Science* **351**, 1154–1155 (2016).
10. Palm, G. J. et al. Structure of the plastic-degrading *Ideonella sakaiensis* MHETase bound to a substrate. *Nat. Commun.* **10**, 1717 (2019).
11. Han, X. et al. Structural insight into catalytic mechanism of PET hydrolase. *Nat. Commun.* **8**, 2106 (2017).
12. Joo, S. et al. Structural insight into molecular mechanism of poly(ethylene terephthalate) degradation. *Nat. Commun.* **9**, 382 (2018).
13. Austin, H. P. et al. Characterization and engineering of a plastic-degrading aromatic polyesterase. *Proc. Natl Acad. Sci. USA* **115**, E4350–E4357 (2018).
14. Taniguchi, I. et al. Biodegradation of PET: current status and application aspects. *ACS Catal.* **9**, 4089–4105 (2019).
15. Brueckner, T., Eberl, A., Heumann, S., Rabe, M. & Guebitz, G. M. Enzymatic and chemical hydrolysis of poly (ethylene terephthalate) fabrics. *J. Polym. Sci. A* **46**, 6435–6443 (2008).
16. Vertommen, M. A., Nierstrasz, V. A., van der Veer, M. & Warmoeskerken, M. M. Enzymatic surface modification of poly(ethylene terephthalate). *J. Biotechnol.* **120**, 376–386 (2005).
17. Wei, R. et al. Biocatalytic degradation efficiency of postconsumer polyethylene terephthalate packaging determined by their polymer microstructures. *Adv. Sci.* **6**, 1900491 (2019).
18. Ronkvist, A. S. M., Xie, W., Lu, W. & Gross, R. A. Cutinase-catalyzed hydrolysis of poly(ethylene terephthalate). *Macromolecules* **42**, 5128–5138 (2009).
19. Zimmermann, W. & Billig, S. Enzymes for the biofunctionalization of poly(ethylene terephthalate). *Adv. Biochem. Eng. Biotechnol.* **125**, 97–120 (2010).
20. Kitadokoro, K. et al. Crystal structure of cutinase Est119 from *Thermobifida alba* AHK119 that can degrade modified polyethylene terephthalate at 1.76 Å resolution. *Polym. Degrad. Stabil.* **97**, 771–775 (2012).
21. Chen, S., Su, L., Chen, J. & Wu, J. Cutinase: characteristics, preparation, and application. *Biotechnol. Adv.* **31**, 1754–1767 (2013).
22. Wei, R., Oeser, T. & Zimmermann, W. Synthetic polyester-hydrolyzing enzymes from thermophilic actinomycetes. *Adv. Appl. Microbiol.* **89**, 267–305 (2014).
23. Then, J. et al. Ca^{2+} and Mg^{2+} binding site engineering increases the degradation of polyethylene terephthalate films by polyester hydrolases from *Thermobifida fusca*. *Biotechnol. J.* **10**, 592–598 (2015).
24. Kawabata, T., Oda, M. & Kawai, F. Mutational analysis of cutinase-like enzyme, Cut190, based on the 3D docking structure with model compounds of polyethylene terephthalate. *J. Biosci. Bioeng.* **124**, 28–35 (2017).
25. Sulaiman, S., You, D. J., Kanaya, E., Koga, Y. & Kanaya, S. Crystal structure and thermodynamic and kinetic stability of metagenome-derived LC-cutinase. *Biochemistry* **53**, 1858–1869 (2014).
26. Then, J. et al. A disulfide bridge in the calcium binding site of a polyester hydrolase increases its thermal stability and activity against polyethylene terephthalate. *FEBS Open Bio* **6**, 425–432 (2016).
27. Sowdhamini, R. et al. Stereochemical modeling of disulfide bridges. Criteria for introduction into proteins by site-directed mutagenesis. *Protein Eng.* **3**, 95–103 (1989).
28. Awaja, F. & Pavel, D. Recycling of PET. *Eur. Polym. J.* **41**, 1453–1477 (2005).
29. Barboza Neto, E. S., Coelho, L. A. F., Forte, M. M. C., Amico, S. C. & Ferreira, C. A. Processing of a LLDPE/HDPE pressure vessel liner by rotomolding. *Mater. Res.* **17**, 236–241 (2014).
30. Fullbrook, P. D. in *Glucose Syrups, Science and Technology* (eds Dziedzic, S. Z. & Kearsley, M. W.) 65–115 (Elsevier, 1984).
31. Gusakov, A. V. et al. Design of highly efficient cellulase mixtures for enzymatic hydrolysis of cellulose. *Biotechnol. Bioeng.* **97**, 1028–1038 (2007).
32. Liu, G., Zhang, J. & Bao, J. Cost evaluation of cellulose enzyme for industrial-scale cellulosic ethanol production based on rigorous Aspen Plus modeling. *Bioprocess Biosyst. Eng.* **39**, 133–140 (2016).
33. Mohammad-Khah, A. & Ansari, R. Activated charcoal: preparation, characterization and applications: a review article. *Int. J. Chemtech Res.* **1**, 859–864 (2014).
34. Meyer, D. H. Process for purifying terephthalic acid. US patent 3,288,849 (1966).
35. Merchant Research and Consulting. Sodium sulfate: 2020 world market outlook and forecast up to 2029. https://mcgroup.co.uk/researches/sodium-sulphate (2019).
36. Müller, R. J., Schrader, H., Profe, J., Dresler, K. & Deckwer, W.-D. Enzymatic degradation of poly(ethylene terephthalate): rapid hydrolyse using a hydrolase from *T. fusca*. *Macromol. Rapid Commun.* **26**, 1400–1405 (2005).
37. Sulaiman, S. et al. Isolation of a novel cutinase homolog with polyethylene terephthalate-degrading activity from leaf-branch compost by using a metagenomics approach. *Appl. Environ. Microbiol.* **78**, 1556–1562 (2012).

Reporting summary

Further information on research design is available in the Nature Research Reporting Summary linked to this paper.

Data availability

The authors declare that all data supporting the findings of this study are available within the article, its Extended Data, its Source Data or from the corresponding authors upon reasonable request. The atomic coordinates and structure factors of the reported structures have been deposited in the Protein Data Bank under accession codes 6THS for LCC-S165A and 6THT for ICCG-S165A.

Acknowledgements We thank the ICEO facility of the Toulouse Biotechnology Institute (TBI), which is part of the Integrated Screening Platform of Toulouse (PICT, IBiSA), for providing access to ultrahigh-performance liquid chromatography (UHPLC) and protein-purification equipment; and Toulouse White Biotechnology (TWB, UMS INRAE 1337/UMS CNRS 3582) for providing access to Minibio bioreactors. We acknowledge Carbios (Saint-Beauzire, France), CRITT Bio-Industries (Toulouse, France), Pivert (Venette, France) and Leitat Technological Center (Barcelona, Spain) for their contribution to the purification of the terephthalic acid and for PET and bottle production. We also thank the Structural Biophysics Team of the Institute of Pharmacology and Structural Biology (IPBS, Toulouse, France) for access to the crystallization facility, as well as the ALBA (Barcelona, Spain) and ESRF (Grenoble, France) synchrotrons for data collection. We also acknowledge the use of High-Performance Computing resources on the Occigen (CINES, Montpellier, France) and Curie (TGCC, Paris-Saclay, France) supercomputers as well as on the Computing Mesocenter of Région Midi-Pyrénées (CALMIP, Toulouse, France). This study was supported by Truffle Capital (P. Pouletty) and a grant-in-aid for scientific research (THANAPLAST project, OSEO ISI contract number I 1206040W).

Author contributions I.A., S.D., M. Chateau, V.T. and A.M. designed and directed the research. This work was further conceptualized by G.C., C.M.T., B.D. and J.N. In investigation and validation, E.M.-L., A.G., V.T. and H.T. performed enzyme engineering, purification and variant kinetic analysis. I.A., C.M.T., B.D., S.B. and C.F. performed molecular modelling. S.G. and J.N. carried out structural and physical characterization of variants. M.-L.D., M. Cot, E.G. and E.K. carried out reactions in Minibio reactors. M.D. characterized PET powders. E.G., M.D., M. Chateau and M. Cot developed the scheme for purifying terephthalic acid and supervised the production of PET and bottles. M. Chateau, A.M., I.A., V.T. and S.D. wrote the original draft. All authors reviewed and accepted the manuscript.

Competing interests E.G., M.D., M. Chateau and A.M. are employees of Carbios. V.T. has been an employee of Carbios since January 2019. C.M.T., H.T., V.T., M.-L.D., S.D., I.A., S.B. and A.M. have filed patents WO 2018/011284 and WO 2018/011281 for 'Novel esterases and uses thereof'. H.T., M.-L.D., S.D., A.M., M.D. and M. Chateau have filed patent WO 2017/198786, 'A process for degrading plastic products', for protection of part of the work described herein. Confidentiality agreements prevent them from disclosing any newly submitted declaration of invention. All other authors declare no competing interests.

Additional information
Supplementary information is available for this paper at https://doi.org/10.1038/s41586-020-2149-4.
Correspondence and requests for materials should be addressed to I.A., S.D. or A.M.
Peer review information *Nature* thanks Peter Rem and the other, anonymous, reviewer(s) for their contribution to the peer review of this work.
Reprints and permissions information is available at http://www.nature.com/reprints.

a

Enzyme	Organism of origin	UniprotKB Accession number	Reference of polyester hydrolytic activity	Estimated Tm by DSF (°C) ± s.d.
BTA-hydrolase 1	*Thermobifida fusca*	Q6A0I4	23, 36	70.8 ± 0.0
BTA-hydrolase 2	*Thermobifida fusca*	Q6A0I3	23	67.2 ± 0.3
FsC	*Fusarium solani pisi*	P00590	16	56.2 ± 0.2
Is-PETase	*Ideonella sakaiensis 201-F6*	A0A0K8P6T7	8	46.4 ± 0.2
LCC	Uncultured bacterium	G9BY57	37	84.7 ± 0.2

b

PET substrate	Enzyme	Buffer	Specific activity ($mg_{TAeq}.h^{-1}.mg_{enzyme}^{-1}$) ± s.d.			
			40°C	50°C	60°C	65°C
Gf-PET	Is-PETase	50 mM glycine NaOH pH 9	**0.01 ± 0.00**	n. d.	n. d.	n. d.
Gf-PET	FsC	50 mM glycine NaOH pH 9	**0.07 ± 0.01**	0.02 ± 0.00	n. d.	n. d.
Gf-PET	BTA-hydrolase 1	1 M potassium phosphate pH 8	n. d.	0.79 ± 0.03	2.36 ± 0.34	**2.76 ± 0.70**
Gf-PET	BTA-hydrolase 2	1 M potassium phosphate pH 8	n. d.	0.27 ± 0.04	1.85 ± 0.21	**2.10 ± 0.41**
Gf-PET	LCC	100 mM potassium phosphate pH 8	n. d.	16.20 ± 0.07	59.73 ± 3.17	**93.19 ± 0.29**
Pf-PET	LCC	100 mM potassium phosphate pH 8	n. d.	17.02 ± 1.96	n. d.	**81.85 ± 4.53**

Extended Data Fig. 1 | LCC outperformed all other evaluated PET hydrolases during PET-depolymerization assays. a, Enzymes used here that are reported to hydrolyse PET[8,16,23,36,37]. Melting temperatures (T_m) were assessed by DSF; values correspond to means ± s.d. ($n = 3$). **b**, Hydrolysis of amorphous Gf-PET using equimolar amounts of purified Is-PETase, FsC, BTA-hydrolase 1, BTA-hydrolase 2 or LCC (6.9 $nmol_{protein}\ g_{PET}^{-1}$ and 2 $g_{PET}\ l_{buffer}^{-1}$) in their respective buffers at various temperatures. The highest specific activities obtained are in bold. The specific activity of LCC towards Pf-PET is also shown. Means ± s.d. ($n = 3$) are indicated; n.d., not determined.

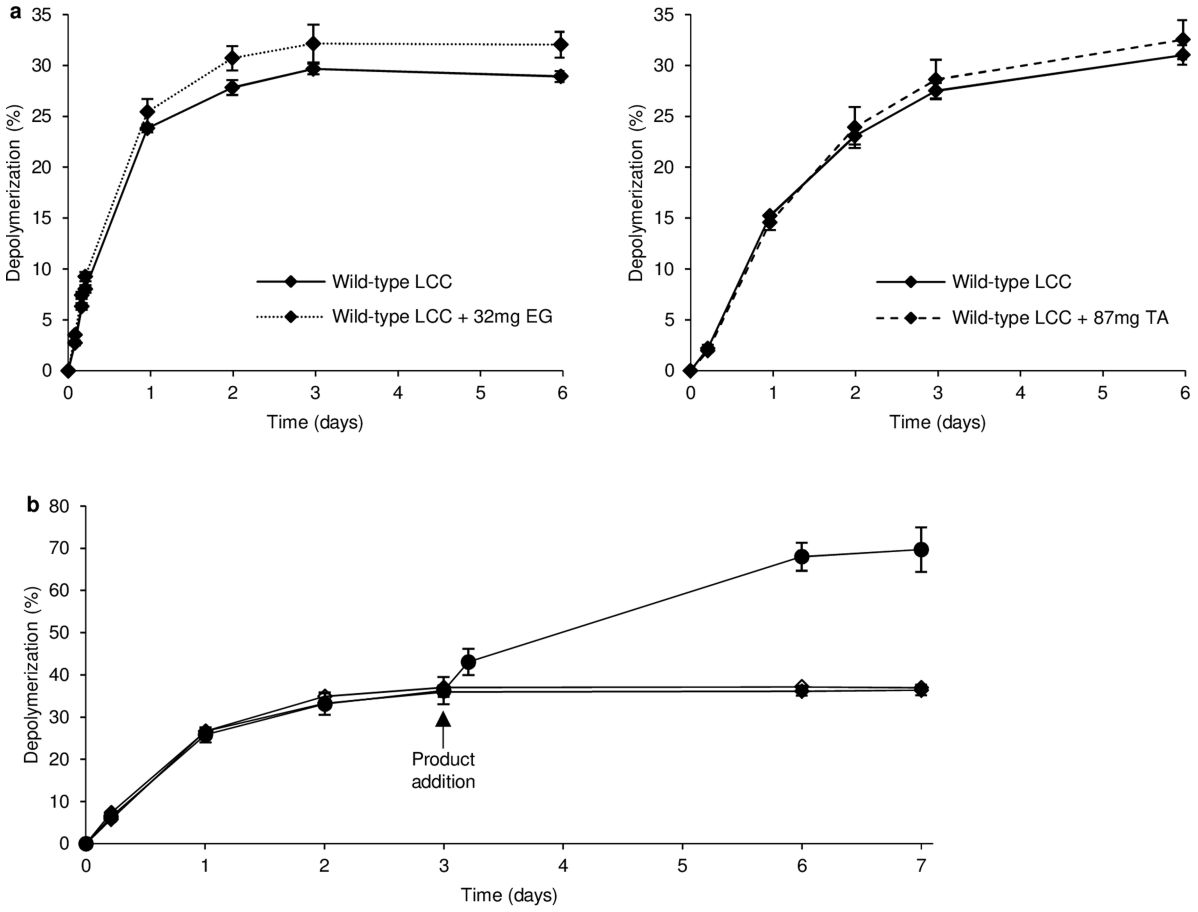

Enzyme	Specific activity ($mg_{TAeq}.h^{-1}.mg_{enzyme}^{-1}$) ± s.d.	Product addition at 3 days	Specific activity after product addition ($mg_{TAeq}.h^{-1}.mg_{enzyme}^{-1}$) ± s.d.
Wild-type LCC	76.8 ± 0.8	n. a.	n. a.
Wild-type LCC	70.6 ± 2.2	100 mg Pf-PET	n. d.
Wild-type LCC	71.7 ± 5.3	0.69 nmol wild-type LCC	76.6 ± 11.7

Extended Data Fig. 2 | The thermostability of LCC at 65 °C is the limiting factor in PET depolymerization. a, Depolymerization of PET by wild-type LCC is not affected by the products of hydrolysis. The graphs compare the kinetics of Pf-PET depolymerization at 65 °C with or without further addition of ethylene glycol (EG; calculated yields (percentages) are obtained from the quantity of terephthalic acid equivalents (TA_{eq}) released during the reaction), and with or without further addition of TA (calculated yields obtained from the quantity of EG released during the reaction). The amount of EG or TA added at reaction initiation corresponds to the quantity of products released with 100% PET depolymerization. Each symbol shows a mean ± s.d. ($n = 3$). **b**, The thermostability of LCC is a limiting factor for the PET-depolymerization yield. No change is observed upon adding 100 mg amorphized Pf-PET after 3 days of reaction at 65 °C (empty diamond) compared with the kinetics of Pf-PET depolymerization by wild-type LCC (filled diamond). However, adding 0.69 nmol of wild-type LCC after 3 days of reaction at 65 °C restarts the previously stopped assay (filled circle) with an identical specific activity to that determined originally (shown in the table). Each symbol represents a mean ± s.d. ($n = 3$); n.a., not applicable; n.d., not determined.

a

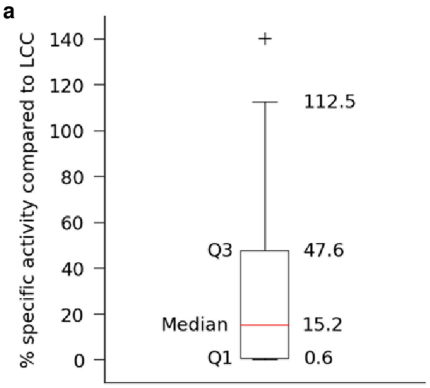

b

Enzyme	Specific activity ($mg_{TAeq}.h^{-1}.mg_{enzyme}^{-1}$) ± s.d.	Specific activity compared to wild-type LCC (%) ± s.d.	Estimated Tm by DSF (°C) ± s.d.	ΔTm (°C) ± s.d.
Wild-type LCC	81.9 ± 5.6	100	84.7 ± 0.2	0
T96M	59.3 ± 3.1	72.5 ± 3.8	87.4 ± 0.2	+2.7 ± 0.2
Y127G	54.5 ± 5.3	66.6 ± 6.5	87.0 ± 0.0	+2.3 ± 0.0
F243I	104.4 ± 5.2	127.5 ± 6.4	81.6 ± 0.0	-3.1 ± 0.0
F243W	96.9 ± 5.6	118.4 ± 6.8	86.1 ± 0.0	+1.4 ± 0.0
N246D	85.4 ± 2.3	104.3 ± 2.9	87.9 ± 0.0	+3.2 ± 0.0
N246M	81.5 ± 1.8	99.6 ± 2.2	88.0 ± 0.2	+3.3 ± 0.2
D238C/S283C	59.2 ± 2.3	72.4 ± 2.8	94.2 ± 0.0	+9.5 ± 0.0
F243I/D238C/S283C	100.2 ± 15.8	122.4 ± 19.3	90.9 ± 0.0	+6.2 ± 0.0
F243W/D238C/S283C	80.0 ± 7.5	97.7 ± 9.1	94.8 ± 0.0	+10.1 ± 0.0
F243I/D238C/S283C/T96M	70.1 ± 1.5	85.7 ± 1.8	94.2 ± 0.0	+9.5 ± 0.0
F243I/D238C/S283C/Y127G	82.0 ± 3.9	100.1 ± 4.8	94.0 ± 0.2	+9.3 ± 0.2
F243I/D238C/S283C/N246D	15.4 ± 2.0	18.8 ± 2.4	86.4 ± 0.0	-0.1 ± 0.0
F243I/D238C/S283C/N246M	96.4 ± 2.9	117.7 ± 3.5	94.5 ± 0.0	+9.8 ± 0.0
F243W/D238C/S283C/T96M	48.2 ± 3.0	58.9 ± 3.7	98.0 ± 0.2	+13.3 ± 0.2
F243W/D238C/S283C/Y127G	75.9 ± 5.9	92.7 ± 7.2	98.0 ± 0.2	+13.3 ± 0.2
F243W/D238C/S283C/N246D	22.9 ± 1.9	28.0 ± 2.4	88.6 ± 0.2	+3.9 ± 0.2
F243W/D238C/S283C/N246M	85.8 ± 4.5	104.9 ± 5.5	98.1 ± 0.0	+13.4 ± 0.0

Extended Data Fig. 3 | Comparative analysis of the LCC variants generated here. a, Boxplot distribution of the saturation results. We produced 209 variants by semi-purification, and determined their respective percentage of specific activity with respect to the wild-type LCC, measured in the same Pf-PET-depolymerization conditions. Q1 and Q3 correspond to the first and third quartiles of the distribution, respectively. The median value is shown as a red line. **b**, Comparison of specific activities and melting temperatures of wild-type LCC and the variants used here. Experiments were performed through preparative production of enzymes followed by a Pf-PET-depolymerization assay (see Supplementary Method 1). Means ± s.d. ($n = 3$) are shown.

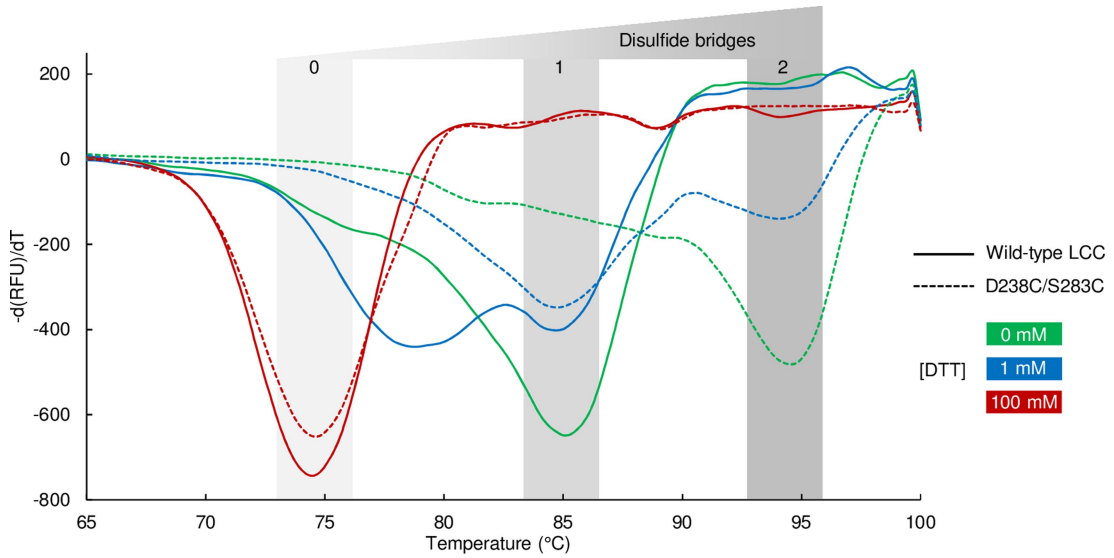

Extended Data Fig. 4 | Formation of an additional disulfide bridge within the D238C/S283C variant of LCC. First derivatives were calculated from DSF thermal denaturation curves for wild-type LCC (solid line) and the D238C/S283C variant (dashed line) in the presence of 0 mM, 1 mM or 100 mM dithiothreitol (DTT). First-derivative peaks correspond to protein melting temperatures. Each curve is representative of a triplicate test. The increasing concentrations of DTT reduced disulfide bridges, resulting in proteins with reduced thermostability. Grey highlighting represents populations with 0, 1 or 2 formed disulfide bridges. Low DTT concentrations (blue curves) were not sufficient to completely reduce all disulfide bridges, resulting in a mixed population of proteins with intermediate melting temperatures. RFU, relative fluorescence units.

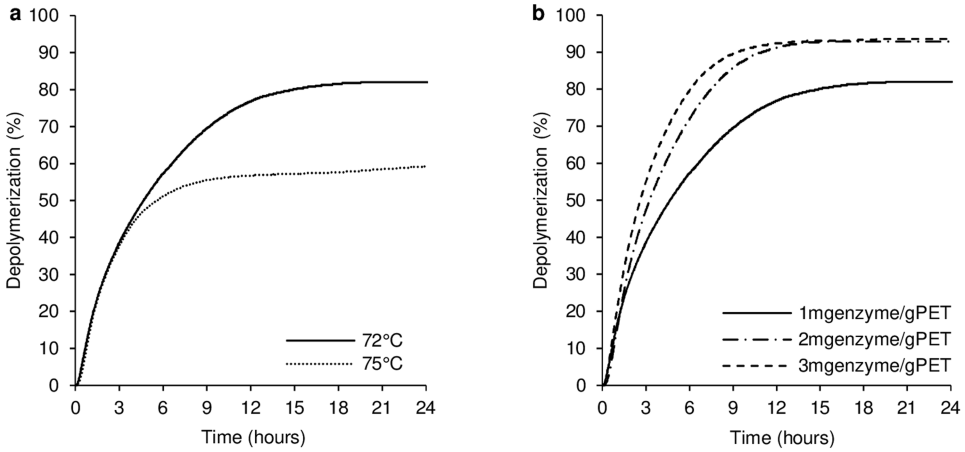

c

Enzyme	Temperature (°C)	Enzyme concentration ($mg_{enzyme}.g_{PET}^{-1}$)	Calculated depolymerization from : NaOH consumption (%)	EG produced (%)	TA_{eq} produced (%)	Residual PET (%)	Initial rate from NaOH consumption ($g_{hydrolyzed\ PET}.L^{-1}.h^{-1}$)
Wild-Type LCC	72	1	52.7	53.3	55.1	53.9	25.7
F243I/D238C/S283C/Y127G	72	1	82.0	84.0	86.0	85.6	31.0
	72	2	92.9	93.3	96.1	95.3	40.3
	72	3	93.6	99.5	96.5	95.1	44.7
	75	1	59.3	60.2	62.7	60.9	34.4
F243I/D238C/S283C/N246M	72	1	78.4	81.9	84.7	81.2	32.2
F243W/D238C/S283C/Y127G	72	1	85.5	89.7	89.0	88.6	30.3
	72	3	92.4	98.8	89.0	92.3	36.2
F243W/D238C/S283C/N246M	72	1	79.6	83.1	81.6	82.5	28.5

Extended Data Fig. 5 | Comparative analysis of the kinetics of PcW-PET depolymerization in Minibio bioreactors by the LCC variants generated here. a, Effect of temperature on PcW-PET depolymerization by the LCC variant F243I/D238C/S283C/Y127G at 72 °C or 75 °C, with 1 $mg_{enzyme}\ g_{PET}^{-1}$. **b**, Effect of enzyme concentration on PcW-PET depolymerization by the LCC variant F243I/D238C/S283C/Y127G at 72 °C with 1 $mg_{enzyme}\ g_{PET}^{-1}$, 2 $mg_{enzyme}\ g_{PET}^{-1}$ or 3 $mg_{enzyme}\ g_{PET}^{-1}$. Percentages of PET depolymerization were calculated on the basis of NaOH consumption. **c**, Comparison of wild-type LCC and variants in assays of PcW-PET depolymerization in Minibio bioreactors. The first two columns show the parameters used during PcW-PET depolymerization (temperature and enzyme concentration). The next four columns show the calculated depolymerization yields (after 24 h), based on either NaOH consumption, EG produced, $TA_{eq.}$ produced, or the weight of residual PET. The last column represents the calculated initial rate of the reaction, based on NaOH consumption.

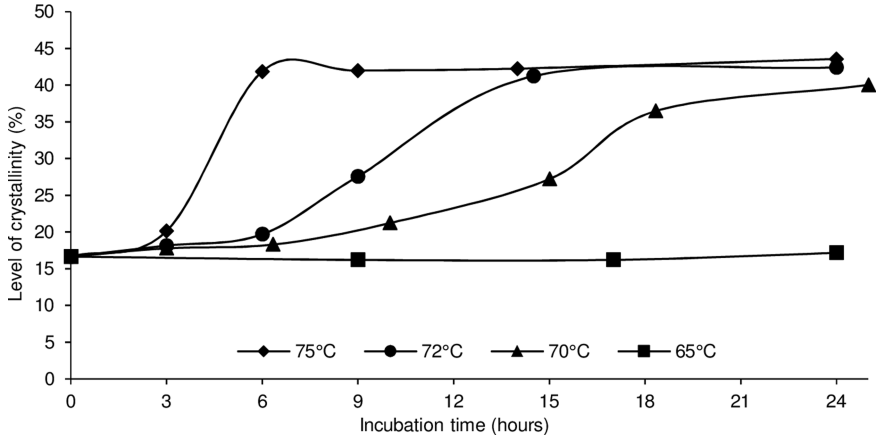

Extended Data Fig. 6 | Kinetics of PET crystallization. Evolution of the crystallinity level of PET (from coloured PcW-PET) at 65 °C, 70 °C, 72 °C and 75 °C.

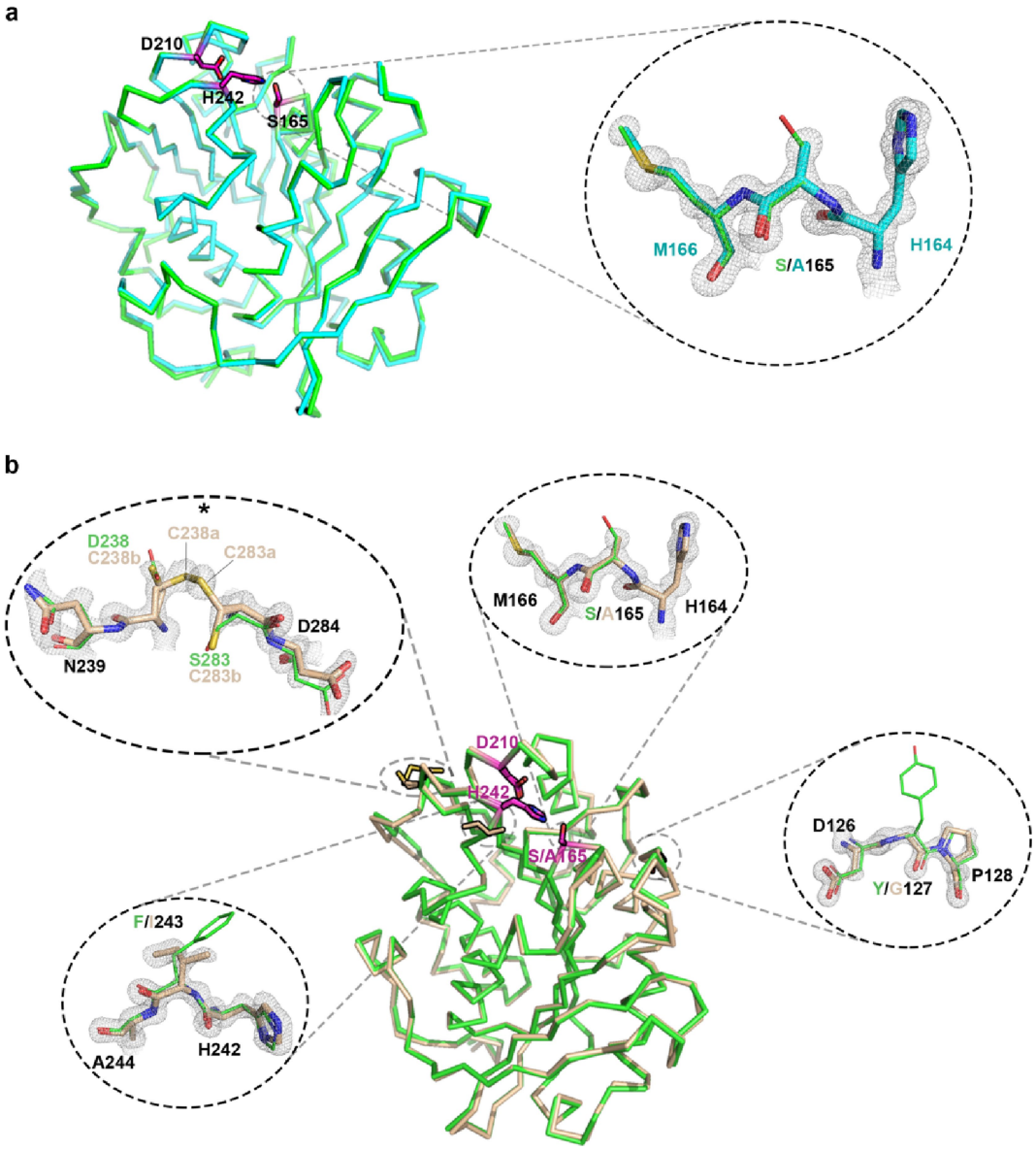

Extended Data Fig. 7 | Overall structures of the catalytic inactive LCC variant S165A and the catalytic inactive F243I/D238C/S283C/Y127G variant S165A. **a**, Left, wild-type LCC (PDB ID 4EB0; green) and the catalytic inactive variant S165A (cyan) are superimposed (with a root mean square deviation (RMSD) of 0.25 Å over 214 Cα atoms). Catalytic residues are represented as magenta rods. The close-up on the right focuses on the catalytic serine (S165) and neighbouring residues. Also shown is an unbiased composite omit map (grey mesh, $2F_o - F_c$) contoured at 2.0σ around residues 164–166. The S165A mutation does not structurally affect the folding of the protein around this position. Moreover, the inactivated enzyme is more liable to crystallize and generate better-quality crystals, so we introduced the S165A mutation to our most efficient LCC variant, namely F243I/D238C/S283C/Y127G (ICCG). **b**, Wild-type LCC (PDB ID 4EB0; green) and the catalytic inactive S165A mutant of the ICCG variant (tan) are superimposed (RMSD = 0.27 Å over 220 Cα atoms). Catalytic (magenta) and mutated (tan) residues are represented as rods. Close-ups show the different mutations and their surrounding residues. Residues from wild-type LCC are represented as thinner rods by comparison with the ICCG variant. Unbiased composite omit maps (grey mesh, $2F_o - F_c$) contoured at 1.5σ are shown. None of the introduced Y127G, S165A, F243I or D238C–S283C (engineered disulfide bridge) mutations affected the overall structure of LCC. The asterisked close-up shows that alternative conformations were observed for the cysteine residues, labelled as conformers a and b.

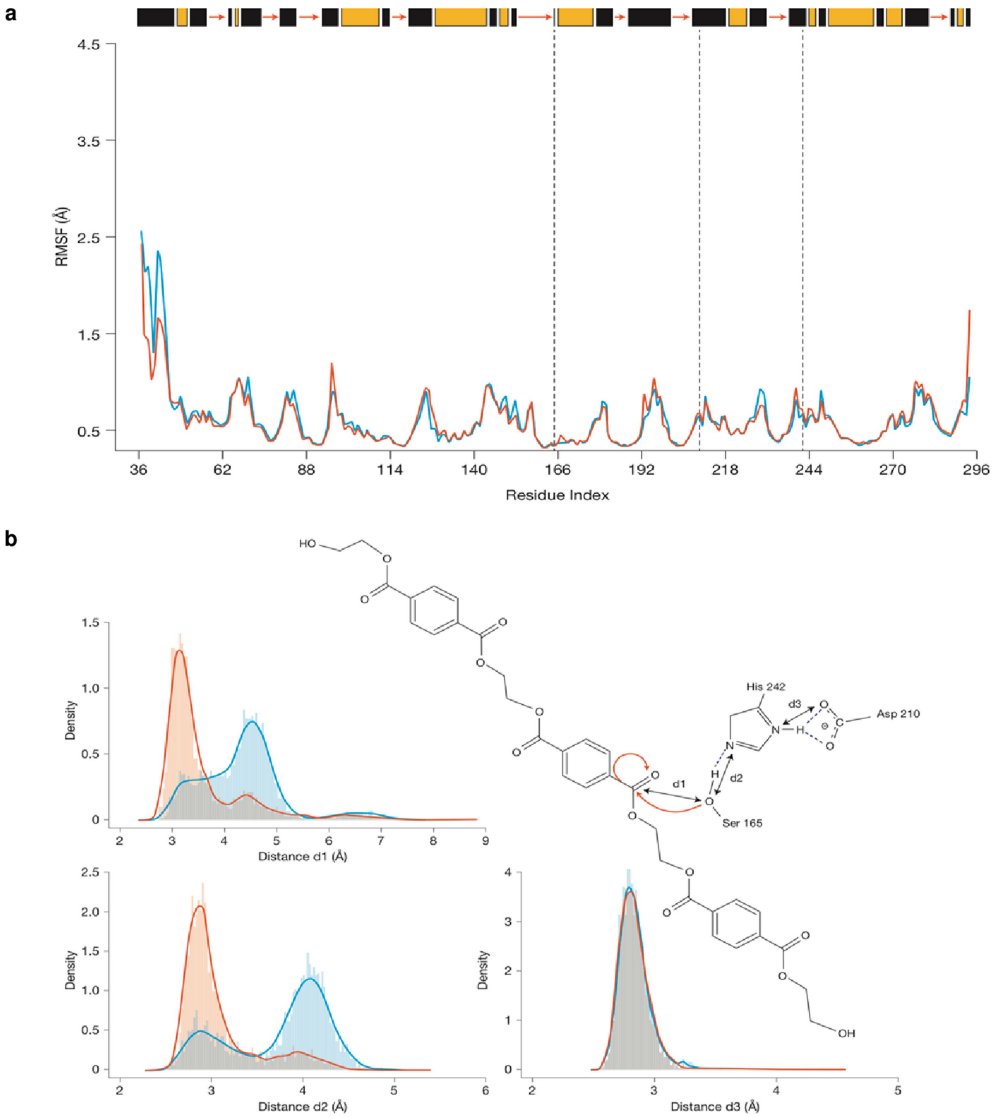

c

Residue donor involved in HB	Residue acceptor involved in HB	HB occurrence in the simulation of the wild-type LCC (%)	HB occurrence in the simulation of the ICCG variant (%)
Ser165 (O-H)	His242 (Nε)	15.2	90.0
His242 (Nδ-H)	Asp210 (OD2)	57.3	89.8

Extended Data Fig. 8 | Analysis of 30-ns molecular-dynamics simulations carried out with wild-type LCC (blue) and the ICCG variant (red). a, Comparison of protein backbone flexibility using average root mean square fluctuations (RMSF) of Cα atoms calculated per residue along molecular-dynamics simulations of enzymes in the apo conformation. The RMSF is linked to the crystallographic B-factor (*B*) as follows: $\mathrm{RMSF} = \sqrt{\left(\frac{3B}{8\pi^2}\right)}$. Red arrows, β-strands; black rectangles, α-helices; yellow rectangles, loops in the X-ray crystal structure of the wild-type LCC (PDB ID 4EB0); dashed lines, positions of catalytic residues. **b**, Monitoring of key catalytic interatomic distances that characterize the catalytic events occurring during molecular-dynamics simulations of enzymes in complex with the model substrate 2-HE(MHET)$_3$. At the right is a representation of the catalytic triad (residues S165 (Ser 165), H242 (His 242) and D210 (Asp 210)) and 2-HE(MHET)$_3$, highlighting three relevant interatomic distances (d1, d2, d3). The three graphs show the distributions of these three distances over the first 30 ns of molecular-dynamics simulations of wild-type and ICCG LCC in complex with 2-HE(MHET)$_3$ (represented as histograms and Gaussian kernel densities), starting from the same initial conformation. Red arrows show changes occurring during the nucleophilic attack of the catalytic serine on the substrate reactive centre; dashed blue lines show hydrogen bonds that assist the catalytic mechanism. The graphs highlight the favoured catalytically productive state adopted by 2-HE(MHET)$_3$ in variant ICCG. Substantial changes are observed for d1 and d2. Whereas ICCG mainly sampled conformations near the catalytically productive state (average d1 is approximately 3.2 Å; average d2 is approximately 2.8 Å), the wild-type LCC showed a pronounced bimodal distribution with the major conformational population centred on higher distance values, indicating less efficient catalysis. Overall, along the first 30 ns of simulations of these enzymes in complex with 2-HE(MHET)$_3$, the average distance separating the substrate cleavage site from the catalytic serine (S165) hydroxyl oxygen was substantially shorter in ICCG than in parental LCC, suggesting that formation of the covalent intermediate during catalysis would be facilitated. **c**, Occurrence of key hydrogen bonds (HBs) between pairs of catalytic residues. The third and fourth columns show the proportion of snapshots in which an HB interaction is observed between the pairs of catalytic residues S165/H242 and H242/D210 during the first 30 ns of simulations. The higher occurrence of HBs in the ICCG simulation between the S165 hydroxyl oxygen and the catalytic H242 ε nitrogen could assist in the abstraction of the S165 hydroxyl hydrogen by H242, and thus enhance the catalytic performance of this variant.

Extended Data Table 1 | Sequence analysis of eight prokaryotic cutinase homologues of known crystal structure

Enzyme	PDB ID	%ID	Catalytic & Putative 3PET binding residues															
			SITE −2						SITE −1							SITE +1		
LCC Leaf branch metagenome	4eb0	100	Y95	F125	Y127	M166	W190	A213	G94	T96	H164	S165	D210	V212	H242	S101	F243	N246
Is-PETase *Ideonella sakaiensis*	5xg0	49.2	Y58	L88	Q90	M132	W156	A180	G57	T59	W130	S131	D177	I179	H208	S64	S209	N212
TfCut2 *Thermobifida fusca*	4cg2	59.9	Y60	L90	Q92	M131	W155	A179	G59	T61	H129	S130	D176	I178	H208	S66	F209	N212
Thc Cut1 *Thermobifida cellulosilytica*	5lui	60.3	Y61	L91	Q93	M132	W156	A180	G60	T62	H130	S131	D177	I179	H209	S67	F210	N213
Thc Cut2 *Thermobifida cellulosilytica*	5luj	59.1	Y61	L91	Q93	M132	W156	A180	G60	T62	H130	S131	D177	I179	H209	S67	F210	N213
Est119 *Thermobifida alba*	3wyn	61.2	Y99	L129	Q131	M170	W194	A218	G98	T100	H168	S169	D215	I217	H247	S105	F248	N251
Cut190 variants *Saccharomonosporas viridis*	4wfj, 5zno	56.9	F106	L136	Q138	M177	W201	A225	G105	T107	H175	S176	D222	I224	H254	S112	F255	N258
PmC *Pseudomonas mendocina*	2fx5	24.7	T58	N86	G88	Q127	Y150	A179	G57	G59	H125	S126	D176	I178	H206	T64	F207	V210
Relative Shannon entropy			0.36	0.70	0.47	0.17	0.20	0.23	0.005	0.49	0.19	0.005	0.007	0.36	0.002	0.63	0.43	0.55

The enzymatic substrate-binding site can be subdivided into three subsites (−2, −1, +1), each in contact with the MHET units numbered relative to the scissile ester bond. For LCC, catalytic residues are underlined with a solid line, and residues involved in formation of the oxyanion hole are underlined with a dotted line. Column 3 (%ID) indicates the percentage of sequence identity relative to wild-type LCC. Columns 4–6 (Site −2, Site −1 and Site +1) show the amino acid residues in contact with the 2-HE(MHET)$_3$ substrate, as well as the catalytic serine and the histidine from the first shell and the aspartate from the second shell (S165, H242 and D210 in LCC). The bottom row shows the relative Shannon entropy, calculated from a multiple sequence alignment of 609 LCC homologues using the software tool SEQUESTER. We found 15 amino acid residues in the first contact shell and selected 11 for mutagenesis experiments (the essential catalytic S165 and H242 residues, the conserved M166 residue forming the oxyanion hole involved in stabilization of the tetrahedral reaction intermediate, and the highly conserved G94 residue were excluded when Y95, the second residue of the oxyanion hole, was selected for mutagenesis, as it is less conserved than M166).

Extended Data Table 2 | Data collection and refinement statistics

	LCC Y127G-S165A-D238C-F243I-S283C (PDB 6THT)	LCC S165A (PDB 6THS)
Data collection		
Space group	P 63	P 63
Cell dimensions		
a, *b*, *c* (Å)	109.41, 109.41, 35.18	109.60, 109.60, 35.28
α, β, γ (°)	90, 90, 120	90, 90, 120
Resolution (Å)	32.98 - 1.14 (1.18 - 1.14)	47.46 - 1.10 (1.13 - 1.10)
R_{merge}	0.09 (0.95)	0.06 (0.62)
$I / \sigma I$	11.80 (1.97)	18.06 (3.27)
Completeness (%)	99.98 (99.99)	99.60 (97.52)
Redundancy	9.5 (9.1)	12.7 (12.0)
CC1/2	0.99 (0.75)	0.99 (0.91)
Refinement		
Resolution (Å)	32.98 - 1.14 (1.18 - 1.14)	47.46 - 1.10 (1.13 - 1.10)
No. reflections	87452 (8676)	98540 (9813)
R_{work} / R_{free}	0.11 (0.18) / 0.13 (0.19)	0.13 (0.30) / 0.16 (0.32)
No. atoms		
Protein	1976	1982
Imidazole	5	-
Glycerol	6	-
Citrate	13	-
Dioxane	-	6
Water	299	290
B-factors		
Protein	15.88	14.93
Imidazole	10.95	-
Glycerol	17.00	-
Citrate	23.43	-
Dioxane	-	14.44
Water	28.22	28.84
R.m.s. deviations		
Bond lengths (Å)	0.019	0.016
Bond angles (°)	1.83	1.76

nature research

Corresponding author(s): Alain MARTY

Last updated by author(s): Feb 5, 2020

Reporting Summary

Nature Research wishes to improve the reproducibility of the work that we publish. This form provides structure for consistency and transparency in reporting. For further information on Nature Research policies, see Authors & Referees and the Editorial Policy Checklist.

Statistics

For all statistical analyses, confirm that the following items are present in the figure legend, table legend, main text, or Methods section.

n/a	Confirmed	
☐	☒	The exact sample size (*n*) for each experimental group/condition, given as a discrete number and unit of measurement
☐	☒	A statement on whether measurements were taken from distinct samples or whether the same sample was measured repeatedly
☐	☒	The statistical test(s) used AND whether they are one- or two-sided *Only common tests should be described solely by name; describe more complex techniques in the Methods section.*
☒	☐	A description of all covariates tested
☒	☐	A description of any assumptions or corrections, such as tests of normality and adjustment for multiple comparisons
☐	☒	A full description of the statistical parameters including central tendency (e.g. means) or other basic estimates (e.g. regression coefficient) AND variation (e.g. standard deviation) or associated estimates of uncertainty (e.g. confidence intervals)
☐	☒	For null hypothesis testing, the test statistic (e.g. *F*, *t*, *r*) with confidence intervals, effect sizes, degrees of freedom and *P* value noted *Give P values as exact values whenever suitable.*
☒	☐	For Bayesian analysis, information on the choice of priors and Markov chain Monte Carlo settings
☒	☐	For hierarchical and complex designs, identification of the appropriate level for tests and full reporting of outcomes
☒	☐	Estimates of effect sizes (e.g. Cohen's *d*, Pearson's *r*), indicating how they were calculated

Our web collection on statistics for biologists contains articles on many of the points above.

Software and code

Policy information about availability of computer code

Data collection

X-Ray data were collected at ALBA using the XALOC beamline (wavelength 0.9791 Å), and at the European Synchrotron Radiation Facility (ESRF, Grenoble, France) using the ID30b beamline (wavelength 0.9762 Å)
Tm were estimated on a Bio-Rad CFX96 real-time PCR system using the Bio-Rad CFX Manager software
Thermal characteristics and crystallinity of PET powders were estimated using a DSC 3 from Mettler Toledo
Chromoleon software was used for acquisition of spectra on Agilent 1200 and Ultimate 3000 UHPLC systems.
Minibio bioreactor parameters were followed and controlled using my-Control bio controller system (Applikon Biotechnology, Delft, The Netherlands)

Data analysis	X-ray data processing, structure determination and analyses were carried using standard software packages including XDS, autoPROC toolbox, Phaser, REFMAC5, Coot, Phenix, Pymol Protein multiple alignement were done using MAFFT version 7.310 Protein signal peptides were predicted with SignalP Relative Shannon entropy measures of amino acid residue type variation at each position in a multiple sequence alignment were calculated using SEQUESTER software tool. MMPBSA.py was used to estimate the relative free energy of binding of the substrate model to the enzyme. AMBER 16 package was used for molecular dynamics simulations with the use of the Berendsen algorithm, the Particle Mesh Ewald algorithm and the SHAKE algorithm. All trajectory analyses were performed with the CPPTRAJ module The Avogadro software version 1.1.1 was used to model the substrate, and the Delaunay/Laguerre tessellation using the VLDP software was used to identify contact shell in substrate/enzyme complex LEaP, propKa, RESP method implemented in the Gaussian 09 software, Amber ff14SB force field UHPLC data were analyzed using Chromoleon software version 6.8 for integration of chromatograms.

For manuscripts utilizing custom algorithms or software that are central to the research but not yet described in published literature, software must be made available to editors/reviewers. We strongly encourage code deposition in a community repository (e.g. GitHub). See the Nature Research guidelines for submitting code & software for further information.

Data

Policy information about availability of data

All manuscripts must include a data availability statement. This statement should provide the following information, where applicable:

- Accession codes, unique identifiers, or web links for publicly available datasets
- A list of figures that have associated raw data
- A description of any restrictions on data availability

Structural coordinates have been deposited into the PDB database. Other data are included in this article. Additional supplementary data are available from the corresponding authors upon request.

Field-specific reporting

Please select the one below that is the best fit for your research. If you are not sure, read the appropriate sections before making your selection.

☒ Life sciences ☐ Behavioural & social sciences ☐ Ecological, evolutionary & environmental sciences

For a reference copy of the document with all sections, see nature.com/documents/nr-reporting-summary-flat.pdf

Life sciences study design

All studies must disclose on these points even when the disclosure is negative.

Sample size	For enzymatical assays with quantitative data and Tm assessment, 3 replicates were performed to determine mean and standard deviation and is stated when relevant.
Data exclusions	No data was excluded.
Replication	All in vitro experiments with explicit standard deviation (SD) were performed in triplicates. Attempts at replication were successful.
Randomization	No data was randomized since it was not applicable for our set of experiments.
Blinding	For kinetics measurements, the analytical team who analyzed the amounts of products released were blind to the samples they were analyzing.

Reporting for specific materials, systems and methods

We require information from authors about some types of materials, experimental systems and methods used in many studies. Here, indicate whether each material, system or method listed is relevant to your study. If you are not sure if a list item applies to your research, read the appropriate section before selecting a response.

Materials & experimental systems

n/a	Involved in the study
☒	☐ Antibodies
☒	☐ Eukaryotic cell lines
☒	☐ Palaeontology
☒	☐ Animals and other organisms
☒	☐ Human research participants
☒	☐ Clinical data

Methods

n/a	Involved in the study
☒	☐ ChIP-seq
☒	☐ Flow cytometry
☒	☐ MRI-based neuroimaging